CFD analyses on the water entry process of a freefall lifeboat

Luofeng Huang[a, *], Sasan Tavakoli[b], Minghao Li[c], Azam Dolatshah[b, d], Blanca Pena[a], Boyin Ding[e] and Abbas Dashtimanesh[f]

[a]Department of Mechanical Engineering, University College London, United Kingdom [b]Department of Infrastructure Engineering, University of Melbourne, Australia [c]Department of Mechanics and Maritime Science, Chalmers University of Technology, Sweden [d] Department of Mechanical and Product Design Engineering, Swinburne University of Technology, Australia [e]School of Mechanical Engineering, University of Adelaide, Australia [f]Estonian Maritime Academy, Tallinn University of Technology, Estonia

Abstract: The launch of lifeboats is commonly completed through freefall dropping from a considerable height, where the lifeboat is released from an inclined skid so that it can obtain a forward speed after being launched. The drop is followed by a water entry process that can induce high impact forces on the hull, which gives a significant risk of structural damages. Ascertaining the water entry impact is therefore a key step of lifeboat design; however, conventional methods have linear assumptions and assess the water impact following a quasi-static manner, which causes these methods to be not fully accurate and ignore some important details. To address this gap, this work developed a model based on Computational Fluid Dynamics to holistically simulate and analyse the process. An overset mesh technique was incorporated to reproduce the entire series of drop, water entry and resurfacing, in which the pressure distribution on the whole hull was obtained and recorded with a sampling frequency of 1000 Hz to ensure the peak impacts can be captured. Full-scale measurements were used to confirm the accuracy of the present computational model. Subsequently, a systematic series of simulations were performed to investigate how the water entry process is influenced by the inclined angle and height at which the lifeboat is dropped. The results show that a higher dropping angle can reduce the pressure impacts, but the dropping angle also dictates the lifeboat's motion pattern during the water entry. It was demonstrated that the best dropping angle is around 70 degrees for the investigated case, since an either too low or too high dropping angle would cause the lifeboat to appear in an undesirable after-launch status. This indicates the great importance to assess the optimal dropping angle for every potential freefall lifeboat launch, and the present work proved an effective approach to perform the task.

Keywords: Lifeboat, freefall, water entry, pressure impact, motion, Computational Fluid Dynamics.

*Corresponding author: ucemlhu@ucl.ac.uk

1. Introduction

When extreme maritime incidents occur, lifeboats are required to be launched from a ship deck or a platform. To save the launch time and provide the lifeboat with an initial momentum, a standard launch procedure is to drop a lifeboat from a considerable height, so the lifeboat experiences a freefall process before approaching the water surface, as shown in Figure 1. During the freefall, the lifeboat accumulates a very high speed, thus the following water entry is fierce, causing significant pressure forces on the lifeboat structure. Therefore, it is essential to assess the water entry impacts and prepare accordingly during the lifeboat design circles.

Figure 1: A lifeboat is about to entry water following its freefall launch (photo credit: VIKING Life-Saving Equipment A/S).

Assessing the water entry process has however been a challenge. Although experiments would be the most reliable method to study the process, in practice it is unrealistic to experimentally evaluate the water pressure over the hull, because that would require the installation of numerous pressure sensors to cover all sensitive hull areas. Consequently, measurements can only be performed at limited locations, which means the assessment would not be holistic. Alternatively, modelling methods can overcome the limitation regarding the number of sensors, but it has been difficult to accurately predict the water-induced pressure on the hull. Taking the Finite Element Analysis method (FEA) as an example, it requires a pressure input on a specific location of the hull surface to perform the associated structural analysis, but FEA itself does not have a reliable source to provide that pressure input. Therefore,

previous FEA studies on water-entry lifeboats were established based on a quasi-static assumption, where the water pressure can be obtained from experiments (again, limited locations), or, estimated based on the formulae of gravitational acceleration and dynamic pressure, i.e. $H = \frac{1}{2}gt^2, v = gt, P = \frac{1}{2}\rho_{water}v^2$, where H is the lifeboat's dropping height, and P is the water pressure that can be calibrated and inputted into FEA (Heggelund et al., 2015; Ringsberg et al., 2017). Unreliable sources of water pressure thus add considerable uncertainties in the following FEA structural analyses. Ringsberg et al. (2017) compared similar modelling methods existing in literature with their experimental data, and they reported that these methods have not equipped with satisfactory accuracies and contain errors as large as 20%.

To ascertain the dynamic variation of pressure during the water entry process has been a long-lasting topic. The research performed by Von Karman (1929) is one of the earliest studies in this field and his purpose at that time was to develop a method that can obtain the impact force on a seaplane landing on water surface. He proposed using momentum variation to compute the hydrodynamic force acting on a bluff body penetrating liquid surface, which is dependent on the speed rate and wetted area. Soon after, Wagner (1932) established another groundwork for modelling a water-entering body, assuming the water to rise as jet flows and hit on the walls of the body. This method considers the water as irrotational flow and is applicable for linear boundary conditions without gravity effects. Wagner's solution has then been derived into different variants and applied to various practical conditions (Korobkin, 2004; Tassin et al., 2014). In general, Wagner's solution can be applied for the computation of loads acting on a body penetrating water, which can then be coupled with structural solutions. This method, however, ignores some hydrodynamic phenomena including the flow separation that typically occurs for wedge bodies, which may cause the modelled flow field to be unrealistic.

An alternative method for the water entry problem is the panel integration method which relies on the potential flow theory, where discretisation methods are used to divide the body into a finite number of surfaces, and then the Froude-Krylov force can be obtained. A representative water entry study using this method was conducted by Zhao and Faltinsen (1993), which is still widely used as a benchmark nowadays. Nonetheless, their solution was presented for a zero-gravity condition, which means it may only physically match with water entry processes that contain a very high vertical acceleration to allow the gravity to be neglected. This method was then extended to take gravity into consideration and adopted for cases of a low vertical acceleration (Sun and Faltinsen, 2007). Wu et al. (2010) combined nonlinear velocity attributes with the potential-flow theory to investigate water entry problems. Yet, this type of potential-flow solution cannot account for viscous and turbulent fluid behaviours, still limits its application within estimates in principle.

To perform detailed engineering analyses, solving the Navier-Stokes equations (with the option to couple a turbulence model) has become a mature industrial solution in recent years, known as

Computational Fluid Dynamics (CFD). CFD has been widely applied to predict fluid behaviours (Pena et al., 2019) and fluid-induced structural loads, motions and deformations (Huang et al., 2019; Dashtimanesh et al., 2020; Tavakoli and Babanin, 2021; Tavakoli et al., 2021). The accuracy of CFD has been reported to be very good for hydrodynamic problems where a solid body interacts with multi-phase flows containing a free surface (Windt et al., 2020; Javanmard et al., 2020; Huang et al., 2020a), with viscous and turbulent flows being well modelled (Khojasteh et al., 2020).

There are two branches of applying CFD to simulate water entry problems, mesh-free methods and mesh-based methods. The geometry complexity has been a challenge for mesh-free methods, e.g. Smoothed Particle Hydrodynamics, which represents the fluid and structure as particles (He et al., 2019; Sun et al., 2019). It is particularly challenging to capture complex geometries and model the boundary effect using particles, thus the engineering applicability of mesh-free methods is limited. Due to this deficiency, although a handful of water entry studies have been performed with mesh-free methods, to date validated models have only considered relatively simple geometries (Gong et al., 2009; Iranmanesh and Passandideh-Fard, 2017; Yang, 2018; Sun et al., 2018).

By contrast, mesh-based methods of CFD, known as the Finite Volume Method (FVM), can well account for complex structures, such as lifeboats. FVM allows to precisely represent a hull geometry inside a computational domain, in which a 3D geometry may be expressed as a closed surface that is in contact with numerous computational cells to fully account for its structural complexity and boundary effect. The fluid fields outside the geometry and inside the computational domain can be obtained through solving the Navier-Stokes equations. However, there is still a challenge of applying FVM to model freefall water-entry problems, resulting from that the geometry will experience a large displacement during the process, and such a displacement has to bring the surrounding fluid cells to move together. In standard FVM, this would induce a severe distortion to the mesh and consequently the simulation would crash. A way to get around this is to consider the relative speed. For example, when a ship is advancing in calm water, a common treatment is to fix the ship and let the water flow, where the water speed denotes the constant navigating speed of the ship, by which, the fluid mesh can remain intact (Huang et al., 2020b). This “relative speed” treatment is however inapplicable in the lifeboat drop case, because the lifeboat motion is not constant but to-be-solved, meaning that it is impossible to prescribe it as a relative flow against a lifeboat body. Also, this “relative speed” treatment induces the motion solver of standard FVM (known as the 6-DOF solver) to be incapable of accounting for the large added mass due to the lifeboat’s accelerations during the water entry (Veldman et al., 2017).

Therefore, an advanced meshing approach is required to incorporate with CFD+FVM to handle the large displacement of a structure during its freefall and water entry process. One option can be applying the Immerse Boundary Method (IBM). IBM considers the geometry as a closed wall boundary moving in the fluid domain, with its inside fluid cells being deactivated and outside fluid cells being computed.

IBM, however, is known to generate errors due to oversimplifying the boundary-layer effect of the geometry, because there are no specialised boundary cells outside the moving wall (Mittal and Iaccarino, 2005). Zheng et al. (2020) applied IBM to simulate the water entry process of a wedge body; in particular, they applied a ghost-cell algorithm to remedy the inappropriate boundary layer modelling of IBM. Their results agree very well with the benchmark experiments of Yettou et al. (2006), while it remains to be tested whether the ghost-cell algorithm is generic to 3D hull geometries or not. Alongside IBM, another option is to build an overset mesh, where a surrounding mesh is attached to the geometry and moves together. The surrounding mesh only exchanges solutions with the background mesh, instead of causing distortion. The overset technique allows high-order fluid solutions to be obtained in the surrounding mesh, achieving high-fidelity modelling of the water entry problem. Ma et al. (2018) and Chen et al. (2019) validated a series of 2D water-entry geometries using overset. Roy et al. (2019) demonstrated simulations using overset to model the water-entry process of a realistic lifeboat geometry, but the presented mesh is fairly coarse and there is no validation or a detailed investigation.

In this context, the present study aims to develop a valid model to simulate and analyse freefall lifeboats, based on the CFD+FVM+Overset approach. The novelty of this work is to employ full-scale measurements to validate practicalities for building a reliable 3D computational model to holistically simulate a freefall lifeboat's water entry and resurfacing process; in additional, systematic simulations are conducted to investigate the lifeboat response in detail, demonstrating the lifeboat's motions and loads during different stages. Specifically, this work analyses how the water entry process is influenced by the dropping angle and height. These CFD analyses provide valuable insights into the topic, which would be prohibitive to provide using experiments.

The paper is organised as follows: Section 2 introduces the lifeboat geometry and its freefall launch scenario, followed by introducing the computational approach to replicate the case, including theories and practicalities. Section 3 presents verification (grid convergence studies) and validation of the built model, and then use the model to analyse the pressure distribution and motion pattern of the freefall lifeboat with respect to varying dropping angle and height. Section 4 summarises this work with its implications.

2. Computational approach

2.1 Lifeboat model and fluid domain

The lifeboat used in this work is a typical DNV standard hull (model number: FF 1000), which was designed by the lifeboat manufacturer Schat-Harding (Heggelund et al., 2015). The main parameters of the lifeboat are given in Table 1 and its body plan can be found in (Ringsberg et al., 2017). The reason for this choice is to validate the present computational work with the available measurement data (Kauczynski et al., 2009; Heggelund et al., 2015).

Table 1: Main particulars of the FF 1000 lifeboat (Ringsberg et al., 2017).

	Symbol	Magnitude
Overall length (m)	L	12.57
Overall beam (m)	B	3.34
Mass (tons)	*m*	16.8
Radius of gyration in pitch (m)	R	3.14

To computationally reproduce the freefall and water entry process, a three-dimensional domain was built within the STAR-CCM+ software, as shown in Figure 2. The domain is filled with water to a depth (D), with air filling the remainder. The lifeboat was initialised at a height above the waterline (H) and rotated to an angle (θ). The height denotes the vertical distance between the water surface and the lowest point of the hull. The x-axis is parallel to the central plane of the boat and the z-axis is positive upwards. At the top boundary of the domain, a static pressure boundary condition is applied to represent atmospheric conditions. The bottom boundary is defined as a no-slip wall to account for the presence of the seabed, while D is set at 100 m so that the water can be considered sufficiently deep to avoid shallow water effects. Other four vertical boundaries are also defined as no-slip walls and placed 50 m away from the boat drop location to avoid any boundary interference.

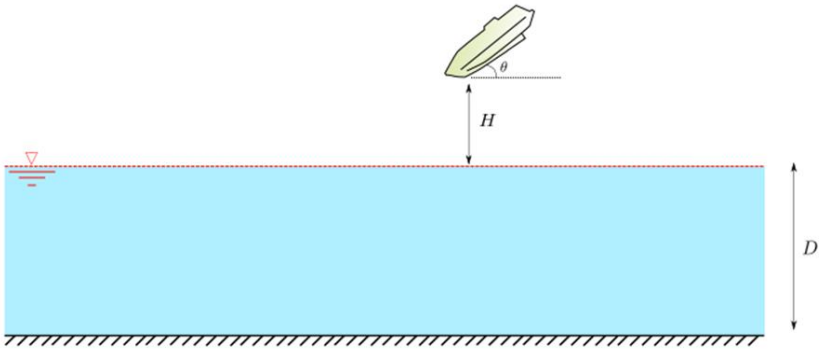

Figure 2: Schematic of the studied problem, showing a lifeboat is about to fall towards water surface from a height of H and with an initial inclining angle of θ.

2.2 Fluid solution

The solution of the fluid domain was obtained by solving the Reynolds-averaged Navier-Stokes (RANS) equations for an incompressible Newtonian fluid:

$$\nabla \cdot \overline{\mathbf{v}} = 0 \tag{1}$$

$$\frac{\partial(\rho\overline{\mathbf{v}})}{\partial t} + \nabla \cdot (\rho\overline{\mathbf{v}}\overline{\mathbf{v}}) = -\nabla\overline{p} + \nabla \cdot \left(\overline{\tau} - \rho\overline{\mathbf{v}'\mathbf{v}'}\right) + \rho g \tag{2}$$

where $\overline{\mathbf{v}}$ is the time-averaged velocity vector and $\mathbf{v}'$ is the fluctuating component, ρ is the fluid density, $\overline{p}$ denotes the time-averaged pressure, $\overline{\tau} = \mu[\nabla v + (\nabla v)^T]$ is the viscous stress term, μ is the dynamic viscosity and g is gravitational acceleration set at 9.81 m/s^2. Since the RANS equations have been adopted to account for the turbulent effects, a turbulence model needs to be applied to close the equations, for which, the Shear Stress Transport (SST) k − ω model (Menter, 1993) was adopted to close the RANS equations. The SST k − ω model has been demonstrated to be a robust RANS turbulence modelling strategy due to its capability to model the flow along boat hulls (Paterson et al., 2003).

The free surface between the air and water was modelled by the Volume of Fluid (VOF) method (Hirt and Nichols, 1981). The VOF method introduces a passive scalar α, denoting the fractional volume of a cell occupied by a specific phase. In this case, a value of α = 1 corresponds to a cell full of water and a value of α = 0 indicates a cell full of air. Thus, the free surface, which is a mix of these two phases, is formed by the cells with 0 < α < 1. The elevation of the free surface along time is obtained by the advection equation of α, expressed as Equation (3). For a cell containing both air and water, its density and viscosity are determined by a linear average according to Equation (4) and Equation (5).

$$\frac{\partial\alpha}{\partial t} + \nabla \cdot (\overline{\mathbf{v}}\alpha) = 0 \tag{3}$$

$$\rho = \alpha\rho_{water} + (1-\alpha)\rho_{air} \tag{4}$$

$$\mu = \alpha\mu_{water} + (1-\alpha)\mu_{air} \tag{5}$$

In this study, ρ_{water} = 1000 kg/m^3, μ_{water} = 8.90×10^{-4} N·s/m^2; ρ_{air} = 1 kg/m^3, μ_{air} = 1.48×10^{-5} N·s/m^2.

2.3 Lifeboat motions

Based on the fluid solution, the hydrodynamic load from fluid acting on the lifeboat, $\boldsymbol{F_h}$, can be obtained as the integration of pressure and viscous force on the hull surface:

$$\boldsymbol{F_h} = \int (-\overline{p}\,\boldsymbol{n} + \overline{\tau}\cdot\boldsymbol{n})\, dS \tag{6}$$

The movement of the lifeboat can be considered as the combination of translation and rotation, which is governed by the rigid-body motion equations in a body-fixed frame based on the mass centre of the boat, $\boldsymbol{G}$–$x'y'z'$:

$$\mathbf{F} = m\frac{d\overrightarrow{V_G}}{dt} \tag{7}$$

$$\mathbf{T} = [\mathrm{J}]\cdot\frac{d\overrightarrow{\omega_G}}{dt} + \overrightarrow{\omega_G}\times([J]\cdot\overrightarrow{\omega_G}) \tag{8}$$

where **F** and **T** are respectively the total force and torque on the lifeboat, induced by gravity and $\mathbf{F_h}$; m and [J] are the mass and inertia moment tensor respectively, and $\mathrm{V_G}$ and ω_G are the translational and rotational velocity vectors of the lifeboat.

2.4 Computational method

The governing equations of the fluid domain were discretised and solved using the Finite Volume Method (Versteeg and Malalasekera, 2007). The process includes two types of discretisation, in space and time respectively. In space, the computational domain is divided into a set of non-overlapping hexahedral cells, known as a mesh; in time, the temporal dimension is split into a finite number of timesteps. The discretisation was performed with 2nd order of spatial accuracy and 1st order of temporal accuracy.

The particular challenge of this case is to handle the large displacement of the lifeboat during the freefall and water entry process. This was tackled by using the overset-mesh technique. Using the overset method, the computational mesh consists of two parts: background mesh and overset mesh, as shown in Figure 3. The background mesh donates the fluid domain which is a fixed Eulerian framework; while

the overset mesh attaches to the lifeboat geometry, moving together with the lifeboat based on its Lagrangian framework (***G***$-x'y'z'$). For every timestep, the boundary cells of the overset mesh obtain fluid solutions from the background mesh; after incorporating with the lifeboat movement, it passes back the updated fluid solution to the background mesh, which achieves a two-way coupling. The two-way process is fully coupled that contains five inner iterations per timestep to match the dynamic and kinetic conditions between the fluid and the lifeboat. In addition, five layers of boundary mesh were applied to the hull geometry to ensure the Y+ value of the whole hull surface is small than 100, which is in line with the corresponding requirement of RANS simulation (ITTC, 2014).

To avoid errors generated by the communication between the background mesh and the overset mesh, the overset part was set to be large enough to contain the whole region where potential water entry is expected to happen. This was achieved by building the overset region to be three times long and five times high of the lifeboat. As the interpolation between overset mesh and background mesh occurs around the outer boundaries of the overset domain (Benites-Munoz et al., 2020), a sufficiently large overset domain can avoid the interpolation to occur in the locations of water-lifeboat interaction; this treatment significantly improves the accuracy of the present model. The optimal mesh density will be analysed in Section 3.1, which is to minimise the computational cost and meanwhile maintain the accuracy of the model.

The size of each timestep was determined by a prescribed Courant number (Co) value, according to the expression:

$$\mathrm{Co} = \frac{v_n \Delta t}{\Delta x} \tag{9}$$

where Δt denotes the time step size, v_n is the flux speed through the shared face between two neighbouring cells, and Δx is its distance between the centres of the two cells. To capture sufficient details for a water entry problem, Co is kept smaller than 0.3 for the computational domain, according to the analyses of Muzaferija (1999). Based on this index, during the mesh sensitivity tests reported in Section 3.1, the timestep size is varied according to the mesh density of every test set. In this way, it is avoidable to do a timestep-size study for every tested mesh.

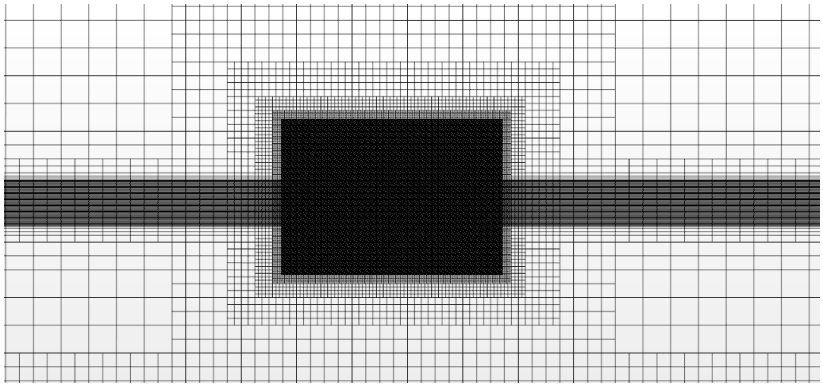

(a) Background

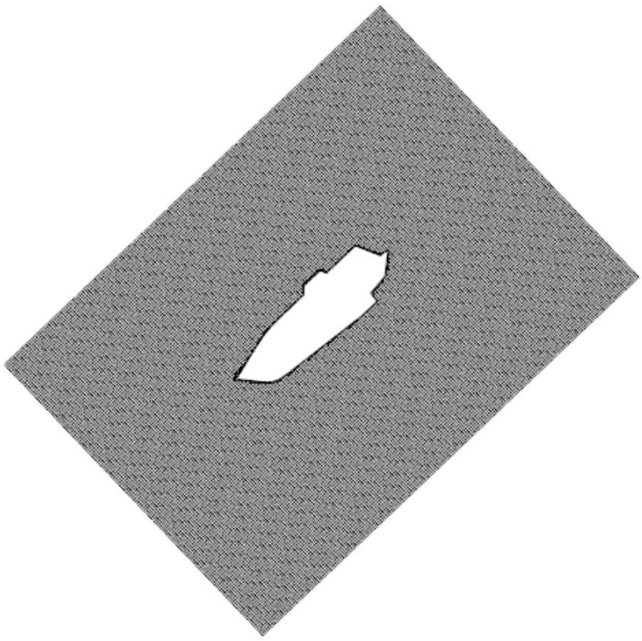

(b) Overset

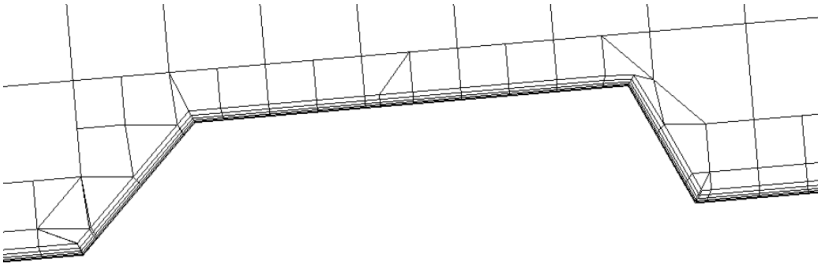

(c) Zoom-in overset

Figure 3: Mesh layout of the model: local refinements are applied in the free-surface and water-entry regions of the background mesh, as well as near-hull layers of the overset mesh. Subfigure (c) manifests the details around the top of the boat, showing boundary mesh layers around the hull.

261

262

3. Results and discussion

The simulation reproduced the entire process of the lifeboat freefall launch and water entry, as presented in Figure 4. After being released, the lifeboat first experiences a freefall, and it approaches the water surface at a very high speed. Then the water starts to apply high resistance/accelerations to the bow of the boat, shown in Figure 4(a), referred to as bow entry. Whilst the bow is slowing down by the water, the stern is still in the air and falling at a higher speed, thus the inertia of the lifeboat causes the stern to rotate and then slam the water surface, as shown in Figure 4(b), referred to as stern entry. Subsequently, the lifeboat continues to fall until the vertical-downwards speed becomes zero, at which point the lifeboat is below the water surface, as shown in Figure 4(c). In the end, the lifeboat is brought resurfacing by its buoyancy, and it has obtained a forward speed resulted from the rotation, as shown in Figure 4(d) and (e). This forward speed initialises the lifeboat to easily move forward and start its mission.

The following contents start by verifying and validating the computational model, where the time-series pressure on the hull surface is compared against measurement data. Subsequently, the validated model is used to perform systematic simulations and analyse the entire process in detail, extracting peak pressure impacts that can occur during different stages of the water entry. In the end, this work investigates how the drop angle and height can influence the structural load and motion pattern of the lifeboat, which suggests the necessity and practices of performing the engineering design using the present approach.

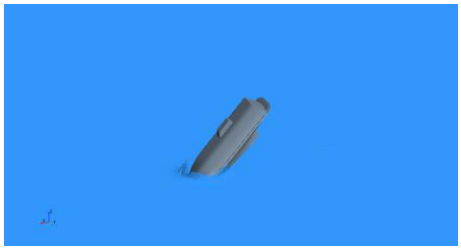

(a) Bow entry, $t = t_0$

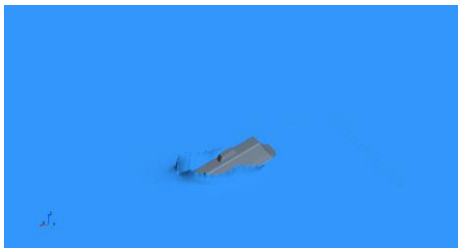

(b) Stern entry, $t = t_0 + 0.2$ s

(c) Submergence, $t = t_0 + 1.1$ s

(d) Resurfacing, $t = t_0 + 1.7$ s

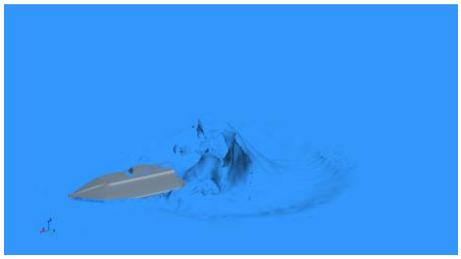

(e) Launch complete, $t = t_0 + 2.4$ s

Figure 4: Simulation illustration for the water entry process of a freefall lifeboat (H = 30 m and θ = 50 °).

303 3.1 Verification and Validation

304 The measurement data used for validation were collected by the Norwegian Marine Technology
305 Research Institute (Kauczynski et al., 2009; Heggelund et al., 2015). The lifeboat was dropped from a
306 height H = 30 m and with an inclining angle θ = 50 °. During the measurement, two pressure sensors
307 were installed respectively at the front and aft regions of the boat. The coordinates of the two sensors
308 are S1 (2.25, 1, 1.1) m, S2 (8.2, 1, 1.1) m, where the *xyz* coordinates count respectively from the tail of
309 the lifeboat, the larboard and the hull bottom, as shown in Figure 5.
310

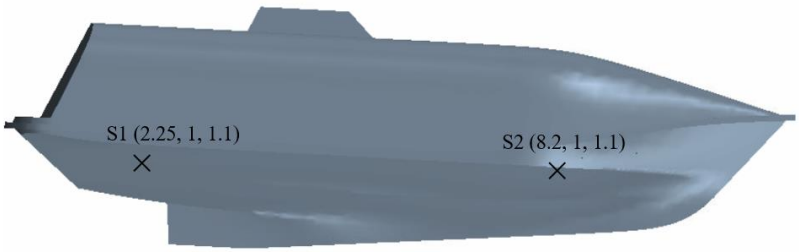

311

312 Figure 5: Locations of two sensors on the lifeboat that applied in the full-scale measurement.

313

314 As the computational cost increases with the cell number, mesh sensitivity tests were first conducted in
315 order to get an accurate solution with as few cells as possible. For this, the mesh density was globally
316 scaled, and four sets of mesh were produced (Coarse, Medium, Fine and Very Fine), respectively having
317 a cell number of 2.7, 3.8, 5.4 and 7.6 million. The time-series pressure at the locations of S1 & S2 were
318 presented using the four sets of meshes, as in Figure 6. It can be seen that the pressure curves converge
319 with the cell number increased, while the improvement between the Fine and Very Fine sets is not
320 distinct. Therefore, the Fine Mesh set was selected to conduct the following analyses, as there is no
321 need to use a higher cell number. According to Co < 0.3, the timestep size corresponding to the Fine
322 Mesh set is 0.001 s.

323 The time-series pressure prediction using the Fine Mesh set is compared with the full-scale
324 measurement data, as shown in Figure 7. In general, it can be seen that the developed model can
325 accurately capture the on-hull pressure along the timeline. Nonetheless, the measurement pressure is
326 observed to decay faster than the computational pressure, which is most likely because the pressure was
327 measured by a plate sensor during the measurement while by a computational cell using CFD. The plate
328 sensor used in experiments covers a certain surface area (approximately 0.1 × 0.1 m^2), and a
329 computational cell is infinitely small. This means that the plate sensor recorded an average pressure for
330 a larger area, thus making the recorded peak pressure decays faster than CFD. This difference however
331 does not influence the prediction of the peak pressure values, which is the utmost parameter and good

agreement between the two methods can be seen. Table 2 provides detailed data of the peak pressure predicted with different mesh sets, alongside the deviations against measurement.

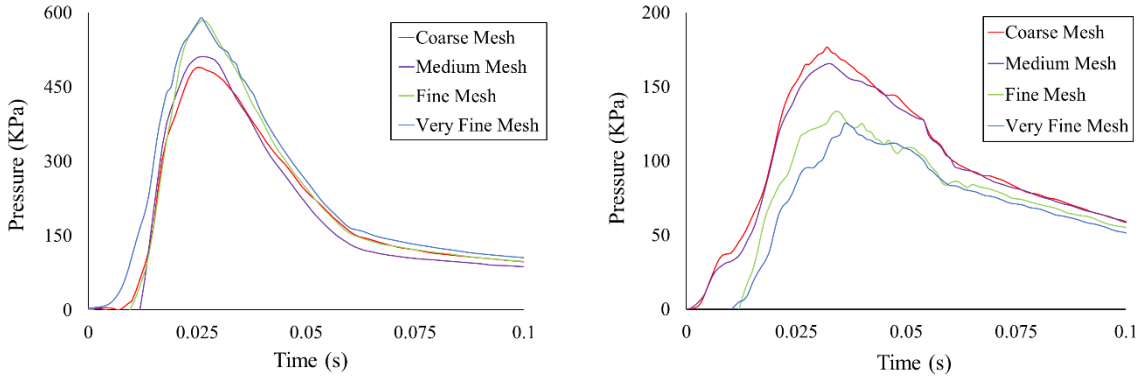

(a) S1: stern sensor (b) S1: bow sensor

Figure 6: Time-series pressure predicted by CFD with different mesh densities (H = 30 m and θ = 50 °).

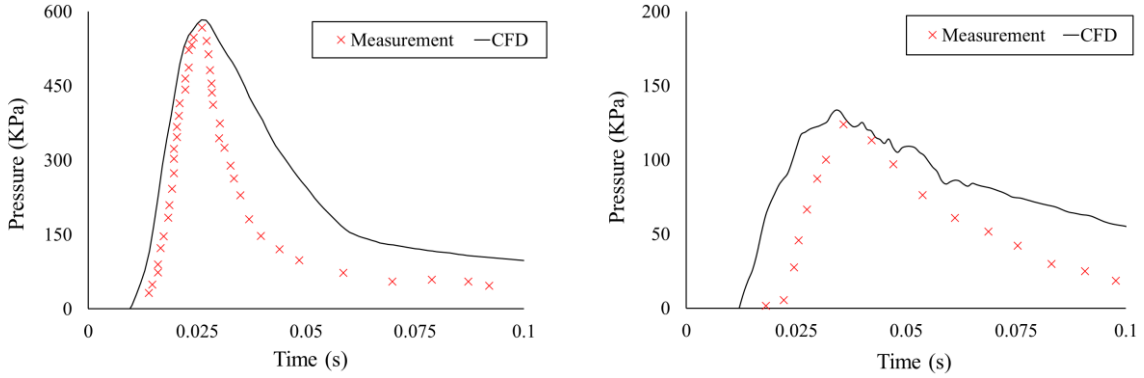

(a) S1: stern sensor (b) S2: bow sensor

Figure 7: Comparison of time-series pressure between full-scale measurements and CFD using the Fine Mesh set (H = 30 m and θ = 50 °).

Table 2: Comparison of peak pressure obtained by CFD using different mesh densities, alongside relative deviations against measurement data.

	Cell number (Million)	S1 peak pressure (KPa)	S2 peak pressure (KPa)
Coarse	2.7	481 (-15.2%)	176 (+38.6%)
Medium	3.8	513 (-9.5%)	165 (+29.9%)
Fine	5.4	587 (+3.7%)	132 (+3.9%)
Very Fine	7.6	589 (+3.8%)	124 (-2.4%)

3.2 Pressure impact

For lifeboat structural design, it is essential to identify the peak pressure impacts during the water entry process. Then the boat scantlings can be determined accordingly during the design stage to secure safety. Also, naval architects may optimise lifeboat geometry by comparing potential hull forms and/or comparing retrofits of a hull form. To serve such purposes, the simulation is able to record water pressure distribution on the entire hull surface and for the entire water-entry process, based on which, three peak pressure impacts were observed, as shown in Figure 8. The pressure distribution in different stages can be read as heat maps on the hull. As in Figure 8(a), when the lifeboat just touching the water, the water applied high pressure on the hull tip to resist the boat's descent, which was the first peak pressure that the hull underwent. Afterwards, whilst the head being slowed down by the water, the rest of the hull body kept falling with a higher downward velocity, which induced the lifeboat to conduct a rotational motion. The rotation caused the bow to slam the water first, followed by the stern to slam, which generated another two peak pressure impacts, respectively presented in Figure 8(b) and Figure 8(c). The stern slamming was stronger than the bow one, as it had a higher rotational radius. No other peak pressure impact was identified after the stern slamming, at which point the vertical velocity of the lifeboat had been mostly attenuated. The above evolution of pressure distribution generally agree with previous water-entry analyses of a 2D wedge geometry, i.e. the peak point moves from the tip to the tail, while always locating around the part penetrating water (Yettou et al., 2007; Bao et al., 2016), but the demonstrated two slamming processes of the 3D lifeboat is distinctive and was unable to be captured by existing analytical theories.

Figure 9 presents the integral force of the lifeboat in the time domain, where the force is split into pressure component and viscous component. It can be seen that the pressure component is at a 10^3 order of the viscous one, which suggests that the viscous component has negligible contribution to the structural load, thus structural designers may focus on analysing the pressure impacts. Although the pressure component is a combination of the slamming force and buoyancy, it can be seen in Figure 9 that, in the first 0.5 seconds, the total magnitude of the pressure component is about ten times of the lifeboat gravity/buoyancy, which means the slamming force governs the lifeboat's motion in the first 0.5 seconds (before it submerges). Whilst the slamming impact on the lifeboat becomes minimal after entering the water, the gravity, buoyancy and viscous forces affect the follow-up motion, in which the gravity and buoyancy dictate the motion in the vertical direction, and the viscous force provides a drag that reduces the lifeboat's horizontal speed.

In summary, the pressure impact of the lifeboat mainly results from the water touching and two slams as shown in Figure 8, which only happens in the initial stage when the lifeboat's speed is very high. Nonetheless, the motion pattern of the lifeboat for the whole process is also of great importance, which is analysed as follows in conjunction with the pressure impact.

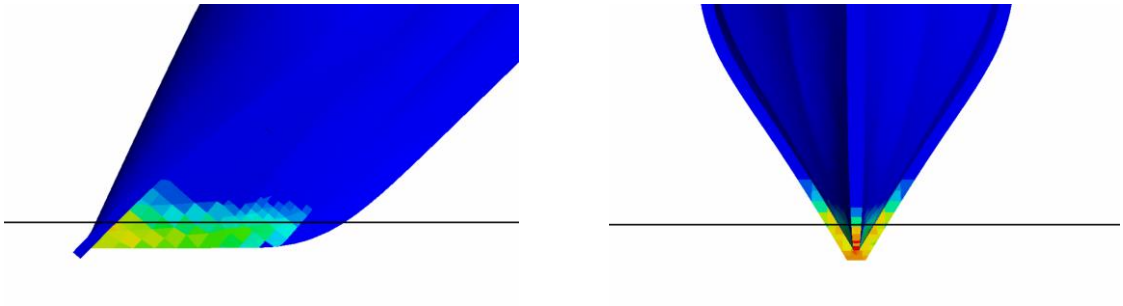

(a) Peak pressure occurs when the lifeboat just touching the water, $t = t_0$

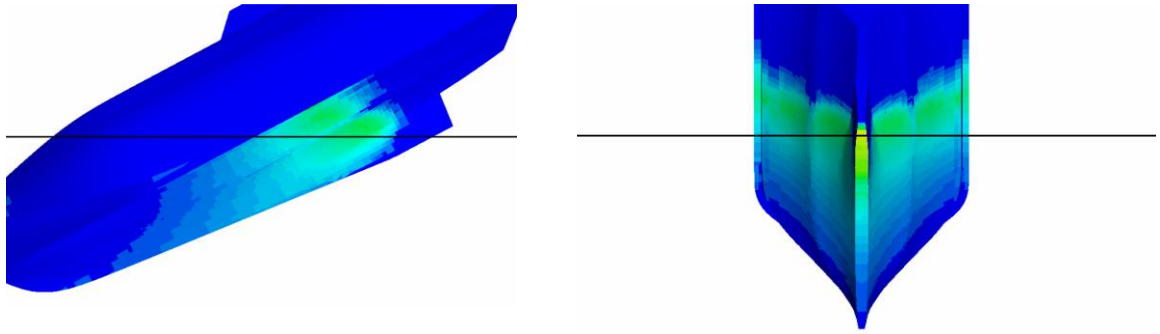

(b) Peak pressure occurs when the bow part slamming the water, $t = t_0 + 0.2$ s

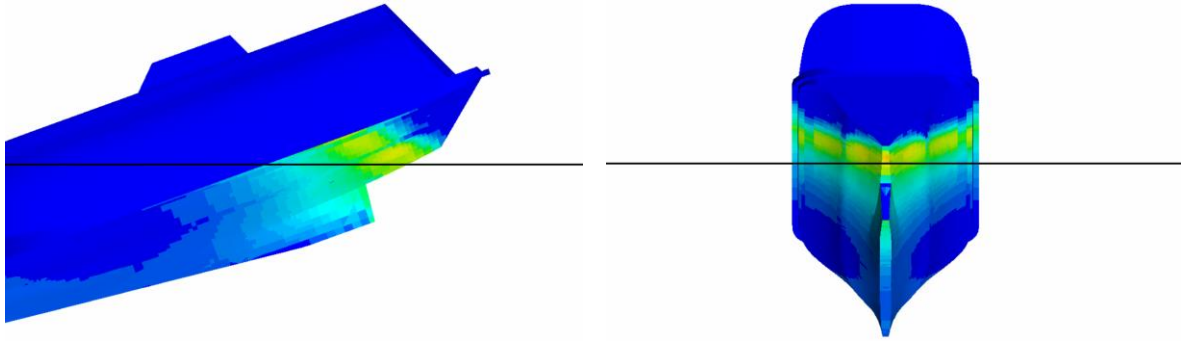

(c) Peak pressure occurs when the stern part slamming the water, $t = t_0 + 0.25$ s

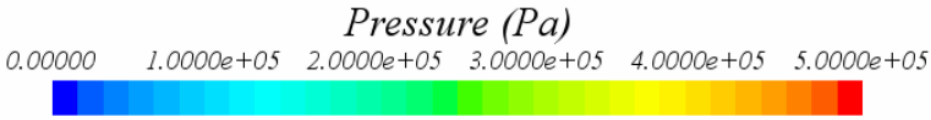

Figure 8: Water pressure impact on the lifeboat, presenting three moments when peak pressure impacts were observed (H = 30 m and θ = 50 °); left and right panels are respectively the profile and bottom view, and the undisturbed waterline is shown as a reference line.

375

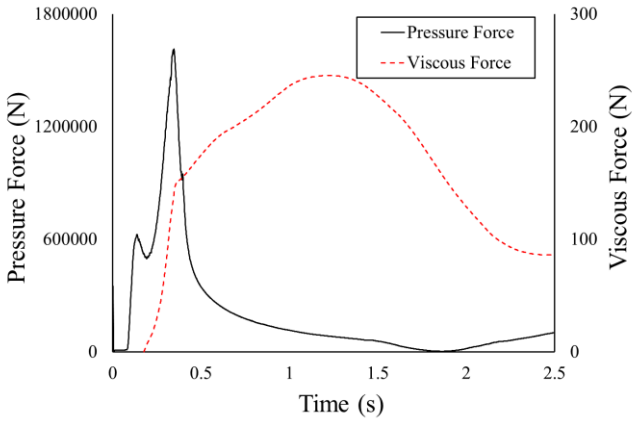

376

377 Figure 9: Total pressure and viscous force on the lifeboat body.

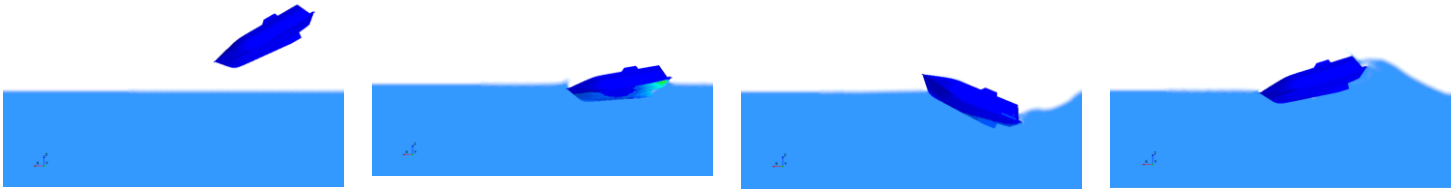

(a) $\theta = 30\,°$

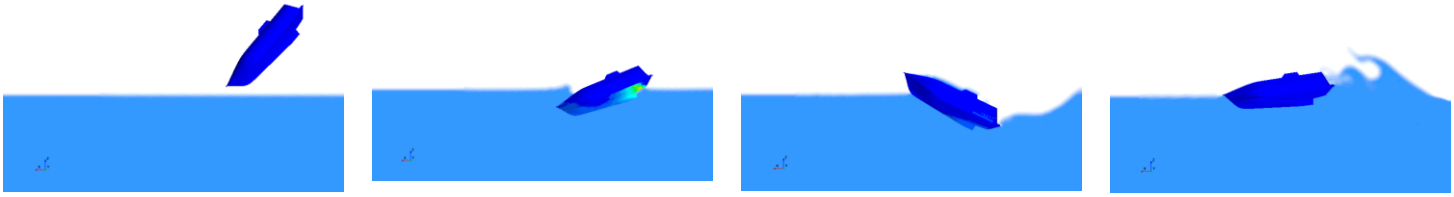

(b) $\theta = 50\,°$

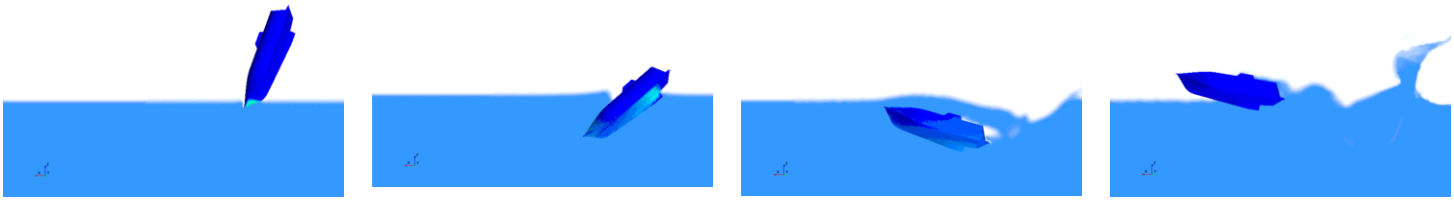

(c) $\theta = 70\,°$

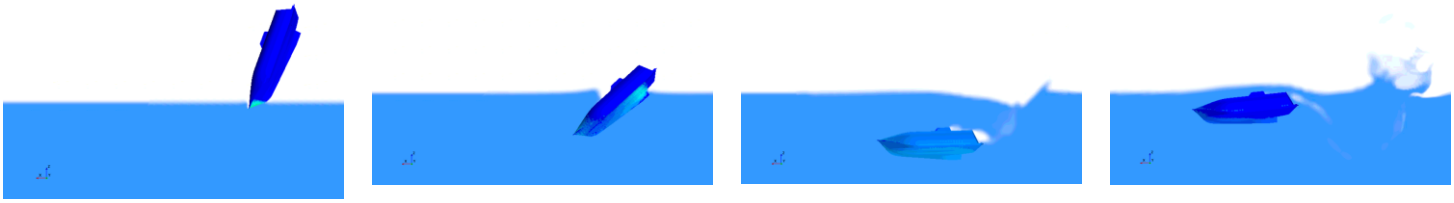

(d) $\theta = 80\,°$

Figure 10: Water entry process of the lifeboat launched at H = 30 m but with different dropping angles; from left to right snapshots were taken at $t = t_0$, $t = t_0 + 0.3$ s, $t = t_0 + 1.2$ s, $t = t_0 + 2.4$ s.

3.3 Influence of dropping angle

This section investigates the influences of the dropping angle on the lifeboat's freefall launch. The aim is to select an optimal dropping angle that leads to a suitable lifeboat status after launched, meanwhile minimising water pressure impacts on the hull. To achieve this, simulations were performed with varying dropping angles ranged between $\theta = 30° - 80°$. The recorded simulations of θ = 30°, 50°, 70° and 80° are shown in Figure 10, since these four are representative cases where significant transitions were observed.

Ideally, the lifeboat is expected to have a positive forward speed after the water entry and resurfacing, which helps it to move away from the parent station and start its mission. Figure 10 demonstrated that the dropping angle has a significant influence on the lifeboat motions during the following water entry. When θ = 30°, the lifeboat presented an up-and-down movement after touching the water surface; along with this motion pattern, the lifeboat could not move a sufficient forward distance from the original horizontal location, which gives a risk that (a) the lifeboat may be pushed back by winds/waves and collide with the parent station (b) the parent station may still be moving and collide with the lifeboat, e.g. the incident of a cargo ship lost control. Thus, such a low dropping angle should be avoided. When θ = 50°, the lifeboat gained a larger forward distance, and the distance increases with the increase of the dropping angle; until θ = 70°, the lifeboat presented an ideal after-launch movement with a desirable forward distance. However, when θ = 80°, the lifeboat dived too deep into the water and the resurfacing was hindered. In this scenario resulted from an excessively high dropping angle, the water imposed the lifeboat a high resistance that would hinder its follow-up mission. The scenarios and risks shown in the simulations agree well with the corresponding general concerns raised in the DNV standard (2009). The records of the lifeboat's horizontal and vertical velocities with varying θ is shown in Figure 11.

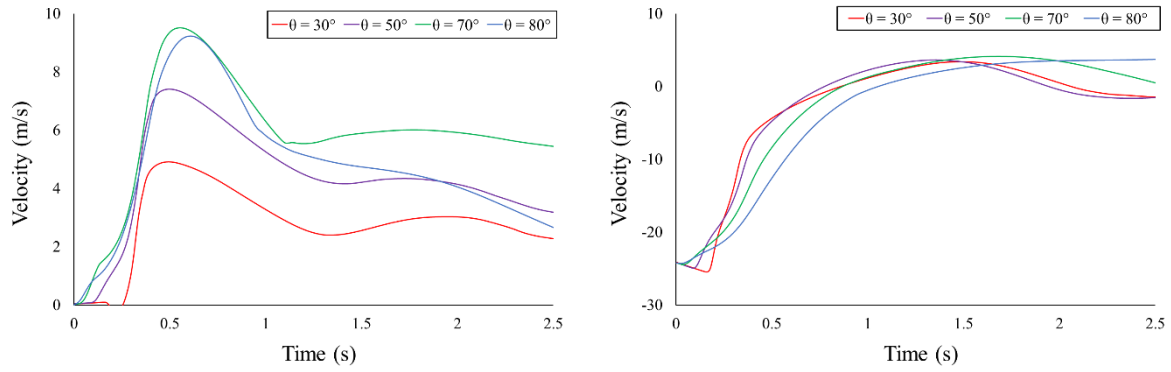

(a) Horizonal velocity (b) Vertical velocity

Figure 11: Time-series velocities of the lifeboat, obtained at H = 30 m but with different dropping angles.

The dropping angle also influences the pressure impacts that the lifeboat undertook during its water entry. Figure 12 presents how the dropping angle influences the peak pressure values during the three significant stages identified in Section 3.2. It can be seen that the peak pressure impacts generally reduce with an increasing dropping angle. This is because a higher dropping angle can sharpen/reduce the contact surface when a lifeboat is diving and effectively weaken the water slamming. In addition, whilst the level of PP2 is relatively low, it shows that PP1 and PP3 are generally of greater importance for the structural assessment.

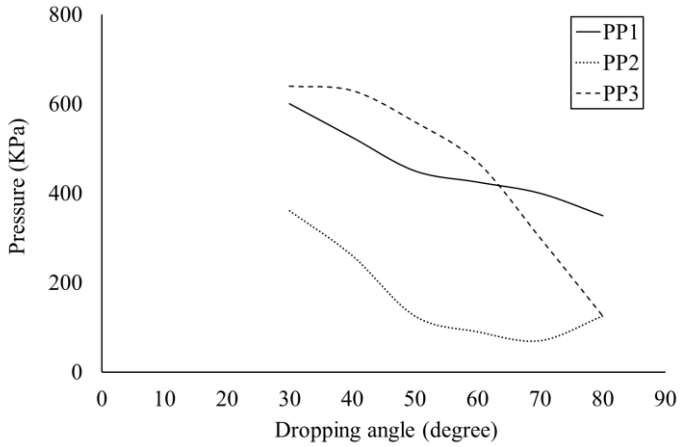

Figure 12: Peak pressure values as a function of the dropping angle (H = 30 m). PP1: the peak pressure value recorded when the lifeboat just touching the water – Figure 8(a); PP2: the peak pressure value recorded during bow entry – Figure 8(b); PP3: the peak pressure value recorded during stern entry – Figure 8(c).

3.4 Influence of dropping height

Further investigations were conducted on the lifeboat dropped at H = 10, 20 and 30 m, and with various θ. Figure 13 presents how the dropping height influences two significant peak-pressure impacts: PP1 – the peak pressure when the lifeboat just touching the water, and PP3 - the peak pressure value recorded during stern entry. It can be seen that PP1 shows a linear relationship with the dropping height, which is similar to the trend of a 2D wedge body entering water (Yettou et al., 2006). In the 2D scenario, the analytical models formulate P to have a linear relationship with H, which makes sense as they both have a linear relationship with v^2 (Mei et al., 1999). However, for PP3, a nonlinear relationship versus the dropping height is shown, which means previous linear analytical models cannot be used to predict such slamming forces on the 3D hull geometry, which is in line with the review of Abrate (2011), indicating the significance to develop such a CFD model for the pressure analyses. This explains the deviation existing in contemporary FEA studies using simplified equations to predict the slamming pressure, as also pointed out by Ringsberg et al. (2017).

Figure 14 presents the lifeboat's after-launch forward speed versus different dropping heights and angles. It can be seen that there exists an optimal dropping angle to achieve a maximal forward speed, and the optimal angle is approximately 70 degree for all the three tested dropping heights (and the pressure impacts are generally at a low level when $\theta \approx 70°$, see Figure 12). When H = 30 m and θ = 70°, the lifeboat can obtain a forward speed of 5.5 m/s after the water entry. For the present lifeboat model equipped with 55 horsepower, an initial speed of 5.5 m/s can save around 7 seconds for it to accelerate. Such a quantity of time can be invaluable during maritime incidents, especially for explosive events. This result highlights the importance of pre-setting the dropping skid at an optimal angle. The after-launch forward speed can still be very sensitive to subtle variations of angles around 70 degrees and it may be different for another lifeboat model. Thus it is recommended to use CFD to subtly change the dropping angle and work out the best setup for each design task, as the lifeboat model and dropping height are normally given.

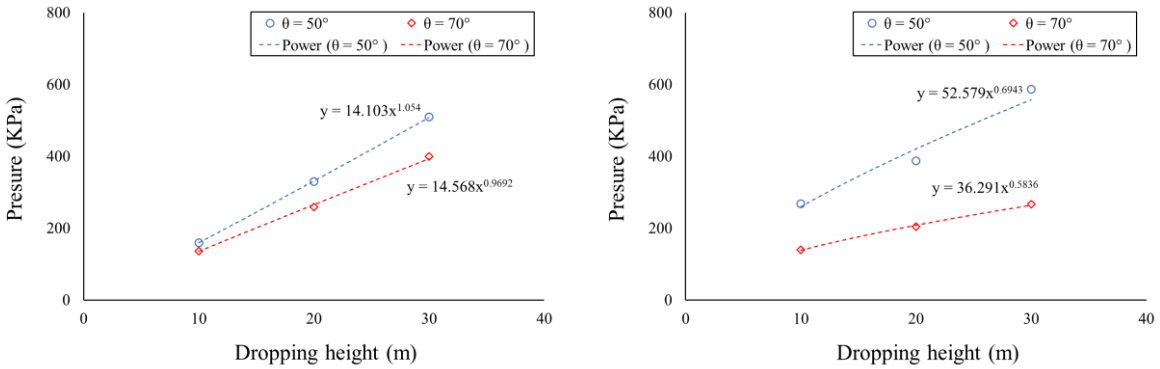

(a) PP1 (b) PP3

Figure 13: Peak pressure values as a function of dropping height.

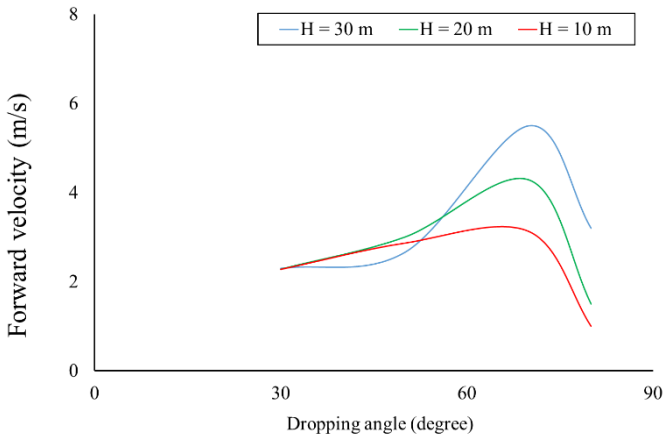

Figure 14: The lifeboat's after-launch forward speed at different dropping heights and angles.

4. Conclusions

This work developed a CFD model to simulate and analyse the water entry process of a freefall lifeboat. The simulation was demonstrated to reproduce the process with high fidelity, and it was validated to have the ability to accurately predict the pressure change on the hull surface. Comparing with contemporary quasi-static methods to predict the water pressure on freefall lifeboats, the present approach offered advantages that (a) the water pressure can be dynamically monitored along the entire timeline, (b) the pressure monitoring can cover the whole hull surface, and (c) offering accurate prediction of hull slamming forces that are not equipped by linear analytical models. These advantages ensure peak pressure impacts to be captured, which is a great improvement to contemporary analyses used by designers.

Furthermore, the freefall launch process was investigated with different dropping angles and heights applied. It was found that a too low dropping angle cannot effectively help the lifeboat move forward and gives it a risk of colliding with the parent station. A higher dropping angle can mitigate this risk and reduce the pressure impacts on the hull, but if the angle is too high, the lifeboat would dive too deep that its further movement would be hindered by water. Therefore, an optimal dropping angle exists for the freefall launch process; by pre-setting a dropping skid at its optimal angle, a lifeboat can obtain a significant initial speed that can help it smoothly set off thus saving seconds of precious time to run away from hazardous events. Therefore, it is crucial to assess the optimal dropping angle for every potential freefall launch task, and the present work demonstrated a convenient approach to do that.

References

Abrate, S., 2011. Hull slamming. Applied Mechanics Reviews 64.

Bao, C.M., Wu, G.X., Xu, G.D., 2016. Simulation of water entry of a two-dimension finite wedge with flow detachment. Journal of Fluids and Structures 65, 44–59.

Benites-Munoz, D., Huang, L., Anderlini, E., Marín-Lopez, J.R., Thomas, G., 2020. Hydrodynamic Modelling of An Oscillating Wave Surge Converter Including Power Take-Off. Journal of Marine Science and Engineering 8, 771.

Chen, H., Qian, L., Ma, Z., Bai, W., Li, Y., Causon, D., Mingham, C., 2019. Application of an overset mesh based numerical wave tank for modelling realistic free-surface hydrodynamic problems. Ocean Engineering 176, 97–117.

Dashtimanesh, A., Tavakoli, S., Kohansal, A., Khosravani, R., Ghassemzadeh, A., 2020. Numerical study on a heeled one-stepped boat moving forward in planing regime. Applied Ocean Research 96, 102057.

DNV, 2009. Offshore standard DNV-OS-E406: Design of free fall lifeboats.

Gong, K., Liu, H., Wang, B., 2009. Water entry of a wedge based on SPH model with an improved boundary treatment. Journal of Hydrodynamics 21, 750–757.

He, M., Gao, X., Xu, W., Ren, B., Wang, H., 2019. Potential application of submerged horizontal plate as a wave energy breakwater: A 2D study using the WCSPH method. Ocean Engineering 185, 27–46.

Heggelund, S.E., Li, Z., Jang, B.-S., Ringsberg, J.W., 2015. Quasi-Static Assessment of Response to Slamming Impact on Free Fall Lifeboats, in: ASME 2015 34th International Conference on

485 Ocean, Offshore and Arctic Engineering. American Society of Mechanical Engineers Digital
486 Collection.
487 Hirt, C.W., Nichols, B.D., 1981. Volume of fluid (VOF) method for the dynamics of free boundaries.
488 Journal of computational physics 39, 201–225.
489 Huang, L., Li, M., Romu, T., Dolatshah, A., Thomas, G., 2020a. Simulation of a ship operating in an
490 open-water ice channel. Ships and Offshore Structures 0, 1–10.
491 https://doi.org/10.1080/17445302.2020.1729595
492 Huang, L., Ren, K., Li, M., Tuković, Ž., Cardiff, P., Thomas, G., 2019. Fluid-structure interaction of a
493 large ice sheet in waves. Ocean Engineering 182, 102–111.
494 Huang, L., Tuhkuri, J., Igrec, B., Li, M., Stagonas, D., Toffoli, A., Cardiff, P., Thomas, G., 2020b. Ship
495 resistance when operating in floating ice floes: A combined CFD&DEM approach. Marine
496 Structures 74, 102817.
497 Iranmanesh, A., Passandideh-Fard, M., 2017. A three-dimensional numerical approach on water entry
498 of a horizontal circular cylinder using the volume of fluid technique. Ocean Engineering 130,
499 557–566.
500 ITTC, 2014. Guidelines: Practical Guidelines for Ship CFD Applications. ITTC Report.
501 Javanmard, E., Mansoorzadeh, S., Mehr, J.A., 2020. A new CFD method for determination of
502 translational added mass coefficients of an underwater vehicle. Ocean Engineering 215, 107857.
503 Kauczynski, W.E., Werenskiold, P., Narten, F., 2009. Documentation of Operational Limits of Free-
504 Fall Lifeboats by Combining Model Tests, Full-Scale Tests, and Computer Simulation, in:
505 ASME 2009 28th International Conference on Ocean, Offshore and Arctic Engineering.
506 American Society of Mechanical Engineers Digital Collection, pp. 669–681.
507 Khojasteh, D., Tavakoli, S., Dashtimanesh, A., Dolatshah, A., Huang, L., Glamore, W., Sadat-Noori,
508 M., Iglesias, G., 2020. Numerical analysis of shipping water impacting a step structure. Ocean
509 Engineering 209, 107517.
510 Korobkin, A., 2004. Analytical models of water impact. European Journal of Applied Mathematics 15,
511 821.
512 Ma, Z.H., Qian, L., Martinez-Ferrer, P.J., Causon, D.M., Mingham, C.G., Bai, W., 2018. An overset
513 mesh based multiphase flow solver for water entry problems. Computers & Fluids 172, 689–
514 705.
515 Mei, X., Liu, Y., Yue, D.K., 1999. On the water impact of general two-dimensional sections. Applied
516 Ocean Research 21, 1–15.
517 Menter, F., 1993. Zonal two equation kw turbulence models for aerodynamic flows, in: 23rd Fluid
518 Dynamics, Plasmadynamics, and Lasers Conference. p. 2906.
519 Mittal, R., Iaccarino, G., 2005. Immersed boundary methods. Annu. Rev. Fluid Mech. 37, 239–261.
520 Muzaferija, S., 1999. A two-fluid Navier-Stokes solver to simulate water entry, in: Proceedings of 22nd
521 Symposium on Naval Architecture, 1999. National Academy Press, pp. 638–651.
522 Paterson, E.G., Wilson, R.V., Stern, F., 2003. General-purpose parallel unsteady rans ship
523 hydrodynamics code: Cfdshipiowa., IIHR Report 432. Iowa Institute for Hydraulic Research.
524 The University of Iowa, Iowa, USA.
525 Pena, B., Muk-Pavic, E., Thomas, G., Fitzsimmons, P., 2019. Numerical analysis of a leading edge
526 tubercle hydrofoil in turbulent regime. Journal of Fluid Mechanics 878, 292–305.
527 Ringsberg, J.W., Heggelund, S.E., Lara, P., Jang, B.-S., Hirdaris, S.E., 2017. Structural response
528 analysis of slamming impact on free fall lifeboats. Marine Structures 54, 112–126.
529 Roy, A.S., Janardhanan, S., Nair, E.M.S., 2019. Structural Response of Free–Fall Lifeboats During
530 Emergencies. International Journal of Recent Technology and Engineering.
531 Sun, H., Faltinsen, O.M., 2007. The influence of gravity on the performance of planing vessels in calm
532 water. Journal of Engineering Mathematics 58, 91–107.
533 Sun, P., Zhang, A.-M., Marrone, S., Ming, F., 2018. An accurate and efficient SPH modeling of the
534 water entry of circular cylinders. Applied Ocean Research 72, 60–75.
535 Sun, Y., Xi, G., Sun, Z., 2019. A fully Lagrangian method for fluid–structure interaction problems with
536 deformable floating structure. Journal of Fluids and Structures 90, 379–395.
537 Tassin, A., Korobkin, A.A., Cooker, M.J., 2014. On analytical models of vertical water entry of a
538 symmetric body with separation and cavity initiation. Applied Ocean Research 48, 33–41.

Tavakoli, S., Babanin, A.V., 2021. Wave energy attenuation by drifting and non-drifting floating rigid plates. Ocean Engineering 226, 108717. https://doi.org/10.1016/j.oceaneng.2021.108717
Tavakoli, S., Huang, L., Babanin, A., 2021. Drift motion of floating bodies under the action of green water. Presented at the Proceedings of ASME 2021 40th International Conference on Ocean, Offshore and Arctic Engineering (OMAE2021).
Veldman, A.E., Seubers, H., van der Plas, P., Helder, J., 2017. Free-surface flow simulations with interactively moving bodies, in: International Conference on Offshore Mechanics and Arctic Engineering. American Society of Mechanical Engineers, p. V002T08A002.
Versteeg, H.K., Malalasekera, W., 2007. An introduction to computational fluid dynamics: the finite volume method. Pearson Education.
Von Karman, T., 1929. The impact on seaplane floats during landing.
Wagner, H., 1932. Über stoß-und gleitvorgänge an der oberfläche von flüssigkeiten. ZAMM-Journal of Applied Mathematics and Mechanics/Zeitschrift für Angewandte Mathematik und Mechanik 12, 193–215.
Windt, C., Davidson, J., Ransley, E.J., Greaves, D., Jakobsen, M., Kramer, M., Ringwood, J.V., 2020. Validation of a CFD-based numerical wave tank model for the power production assessment of the wavestar ocean wave energy converter. Renewable Energy 146, 2499–2516.
Wu, G.-X., Xu, G.-D., Duan, W.-Y., 2010. A summary of water entry problem of a wedge based on the fully nonlinear velocity potential theory. Journal of Hydrodynamics, Ser. B 22, 859–864.
Yang, L., 2018. One-fluid formulation for fluid–structure interaction with free surface. Computer Methods in Applied Mechanics and Engineering 332, 102–135.
Yettou, E.-M., Desrochers, A., Champoux, Y., 2007. A new analytical model for pressure estimation of symmetrical water impact of a rigid wedge at variable velocities. Journal of fluids and structures 23, 501–522.
Yettou, E.-M., Desrochers, A., Champoux, Y., 2006. Experimental study on the water impact of a symmetrical wedge. Fluid Dynamics Research 38, 47.
Zhao, R., Faltinsen, O., 1993. Water entry of two-dimensional bodies. Journal of Fluid Mechanics 246, 593–612.
Zheng, K., Zhao, X., Yang, Z., Lv, C., Duan, S., Lin, W., Fang, Z., 2020. Numerical simulation of water entry of a wedge using a modified ghost-cell immersed boundary method. Journal of Marine Science and Technology 25, 589–608.

View publication stats